Title

Phosphate-triggered ratiometric fluoroimmunoassay based on nanobody-alkaline phosphatase fusion for sensitive detection of 1-naphthol for the exposure assessment of pesticide carbaryl

Journal

Journal of Hazardous Materials, 424(Pt C)

ISSN

0304-3894

Authors

Chen, Zi-Jian
Wu, Hui-Ling
Shen, Yu-Dong
et al.

Publication Date

2022-02-01

DOI

10.1016/j.jhazmat.2021.127411

Peer reviewed

HHS Public Access

Author manuscript

J Hazard Mater. Author manuscript; available in PMC 2023 February 15.

Published in final edited form as:

J Hazard Mater. 2022 February 15; 424(Pt C): 127411. doi:10.1016/j.jhazmat.2021.127411.

Phosphate-triggered ratiometric fluoroimmunoassay based on nanobody-alkaline phosphatase fusion for sensitive detection of 1-naphthol for the exposure assessment of pesticide carbaryl

Zi-Jian Chen[a,1], **Hui-Ling Wu**[a,1], **Yu-Dong Shen**[a,*], **Hong Wang**[a], **Yi-Feng Zhang**[a], **Bruce Hammock**[b], **Zhen-Feng Li**[b,c], **Lin Luo**[a], **Hong-Tao Lei**[a], **Zhen-Lin Xu**[a,*]

[a]Guangdong Provincial Key Laboratory of Food Quality and Safety/ Guangdong Laboratory of Lingnan Modern Agriculture, South China Agricultural University, Guangzhou 510642, China.

[b]Department of Entomology and UCD Comprehensive Cancer Center, University of California, Davis, California 95616, United States.

[c]Guangdong Hengrui Pharmaceutical Co., Ltd., Guangzhou 510799, China.

Abstract

The excessive use of carbaryl has resulted in the risk of its exposure. In this study, we isolated six nanobodies (Nbs) from a camelid phage display library against the biomarker of carbaryl, 1-naphthol (1-NAP). Owing to its characteristics of easy genetic modifications, we produced a nanobody-alkaline phosphatase (Nb-CC4-ALP) fusion protein with good stability. A dual-emission system based ratiometric fluoroimmunoassay (RFIA) for quick and highly sensitive determination of 1-NAP was developed. Silicon nanoparticles (SiNPs) was used as an internal reference and for aggregation-induced emission enhancement (AIEE) of gold nanoclusters (AuNCs), while AuNCs could be quenched by MnO_2 via oxidation. In the presence of ALP, ascorbic acid phosphate (AAP) can be transformed into ascorbic acid (AA), the later can etch MnO_2 to recover the fluorescence of the AuNCs. Based on optimal conditions, the proposed assay showed 220-fold sensitivity improvement in comparison with conventional monoclonal antibody-based ELISA. The recovery test of urine samples and the validation by standard HPLC-FLD demonstrated the proposed assay was an ideal tool for screening 1-NAP and provided technical support for the monitoring of carbaryl exposure.

Keywords

1-Naphthol; Carbaryl; Nanobody; Ratiometric fluoroimmunoassay; Pesticide exposure

1. Introduction

For propose of insect controlling and protection of food security, the usage of pesticide in mordent agriculture is increased. However, the improper and excessive use of pesticide

*Corresponding author: shenyudong@scau.edu.cn; xzlin@scau.edu.cn.

[1]Equal contribution

Conflict of interest The author(s) declare that they have no competing interests.

results in large amounts of pesticide residues (Silver et al., 2016; Zhao et al., 2020) in foods (Hu et al., 2016a; Liang et al., 2021) and environment (Bonvallot et al., 2021; Oates and Cohen, 2011). As a result, both occupational and non-occupational pesticide exposure to human beings might be resulted due to the wide pesticide source (Jacobson et al., 2021; Liu et al., 2015; Oates and Cohen, 2011; Peng et al., 2020). As a common carbamate pesticide, carbaryl is also widely used in mordent agriculture (Didpinrum et al., 2020; Shahdost-fard et al., 2021). Toxicological studies reported that carbaryl showed a variety of toxicity to the human beings, including cytotoxicity, genotoxicity, subchronic neurotoxicity, and even carcinogens and mutagens (Saquib et al., 2021; Shahdost-fard and Fahimi-Kashani and Hormozi-nezhad, 2021; Wang et al., 2014). Therefore, it is necessary to investigate and monitor the carbaryl exposure for risk assessment and forewarning of public health security.

Human biomarkers monitoring was considered as a recognized approach to access the risk of pesticides exposure (Aprea et al., 2002; Bonvallot et al., 2021; Peng et al., 2020; Qin and Yan, 2018; Sinha and Banda, 2018). People who are exposed to carbaryl can rapidly metabolize carbaryl to 1-naphthol (1-NAP), a biomarker of carbaryl (Freire et al., 2021; Maroni et al., 2000; Serdar et al., 2008), and excreted in urine within 24 hours (Berman et al., 2016; Esteve-Romero et al., 2012; Sancho et al., 2003). For the detection of 1-NAP in urine samples, instrumental methods are mainly applied because of the high sensitivity, accuracy, and repeatability. (Bravo et al., 2005; Gaudreau et al., 2016; Petropoulou et al., 2006). Nevertheless, it is a challenge that the assessment of pesticide exposure is limited by high cost, long turnaround time and laboratory procedures (Arcury et al., 2006; Rousis et al., 2017).

In comparison with instrumental methods, immunoassay is an alternative technique for measurement of small organic molecules with the advantages of rapid, sensitive, specific, high-throughput and low-cost (Fu et al., 2021). Kramer et al. (1994) firstly prepared a rabbit polyclonal antibody (pAb) to develop an enzyme-linked immunosorbent assay (ELISA) for 1-NAP. But the sensitivity of the prepared pAb was not satisfactory and the pAb always suffered from batch errors. Previously, we synthesized novel haptens to prepare mouse monoclonal antibody (mAb) with improved sensitivity for 1-NAP analysis (Chen et al., 2020). The mAb can conquer the drawbacks of pAb, but the production of mAb still required animals and had limitation on the modification for further application. Recently, the single variable domain of heavy chain (also called nanobody, Nb) produced from camelids and sharks overcome many pitfalls encountered with conventional extraction reagents. It had the advantages of large quantity production, genetic modifications for improved characteristics as well as easily expressed as multivalent reagents (Bever et al., 2016; Li et al., 2018).

The conventional immunoassays included enzyme-link immunosorbent assay (ELISA), lateral flow immunoassay (LFIA) and fluoroimmunoassay (FIA) are the promising and alternative tools for pesticide metabolite analysis. Among these methods, the FIA showed advantages of high sensitivity, low matrix interference and wide detection range (Hua et al., 2017). However, the sensitivity of conventional mono-signal FIA was limited by the interference of background fluorescence (Jin et al., 2017). Compared with single fluorescent emission strategy, dual-signal based ratiometric FIA (RFIA) with self-calibration

have advantages of anti-background interference, improved robustness and accuracy, and sensitivity towards analytes (Niu et al., 2016; Qu et al., 2019; Yan et al., 2015; Zhu et al., 2021).

Gold nanoclusters (AuNCs) was always employed as fluorescent signal probe, which exhibited advantages of facile synthesis, long lifetime, good stability, and excellent water solubility (Hemmateenejad et al., 2016; Jain et al., 2021; Ji et al., 2018). Moreover, the fluorescence of AuNCs can be amplified by aggregation-induced emission enhancement (AIEE) in presence of positive probe (Liu et al., 2021; Qu and Meng and Zi and You, 2019; Xue et al., 2019; You et al., 2018; You and Tseng, 2019). Amount them, owing to the excellent stability and easy synthesis, fluorescent silicon nanoparticles (SiNPs) was a suitable probe to construct SiNP-AuNC hybrid probe for AIEE. Besides, the fluorescent SiNPs can be used as internal reference to reduce background noise and other interferences (Qu and Meng and Zi and You, 2019; Xue and Qu and Han and Xia and You, 2019). For the signal response of AuNCs, fluorescent quenching performed by oxidizing agent was a sensitive, rapid, and feasible response strategy (Jain and Bhagat and Singh, 2021; Lin et al., 2021; Qu and Meng and Zi and You, 2019). As a nanozyme, MnO_2 nanosheet exhibited excellent oxidase-mimicking activity (Tian et al., 2019; Zhang et al., 2020), which can be utilized for the efficiently quenching of SiNP-AuNC hybrid probe.

In this work, we combine the superiorities of nanobody and the nanomaterials to develop a dual-emission system based RFIA for quick and highly sensitive determination of 1-NAP. The assay was carefully optimized and then used to determine the 1-NAP residues in urine samples. The results were validated by standard HPLC-FLD to confirm the accuracy and reproducibility of the proposed assay.

2. Materials and Methods

2.1 Materials

1-NAP and its analogues were obtained from Energy Chemical Co. Ltd. (Shanghai, China). 3-aminopropyltriethoxysilane, glutathione (GSH), sodium dodecyl sulfate, $HAuCl_4{\cdot}4H_2O$, ascorbic acid, ascorbic acid phosphate (AAP), 3,3',5,5'-tetramethylbenzidine (TMB), and p-nitrophenyl phosphate (pNPP) were supplied by Aladdin Chemical Technology Co., Ltd. (Shanghai, China). Bovine serum albumin (BSA), ovalbumin, and keyhole limpet haemocyanin were purchased from Merck Co. Ltd. (Shanghai, China). Lactoferrin (LF) was supplied by FUJIFILM Wako Pure Chemical Co. Ltd. (Japan). Immunogen (hapten 1-LF) and coating antigen (hapten 1-BSA and hapten 2-BSA) were previously prepared by our laboratory (Chen et al., 2020). The total RNA extraction kit and the first-strand cDNA synthesis kit were purchased from Takara (Dalian, China). The *Sfi*I, *Sac*I, and *Not*I restriction enzymes and T4 DNA ligase were supplied by Thermo Fisher (Shanghai, China). Helper phage M13K07 was purchased from New England Biolabs (MA, USA). The pComb3xss and pET22b vector were gifts from Prof. Bruce Hammock (UC Davis, California, USA). The pET22b-ALP vector was constructed in our laboratory. The *E. coli* TG1 and *E. coli* BL21(DE3) was purchased from Weidi Biotech Co. Ltd. (Shanghai, China) and TransGen Biotech Co. Ltd. (Beijing, China), respectively.

2.2 Instruments

Absorbance was measured at wavelengths of 450 nm or 405 nm using a Multiskan FC microplate reader (Thermo Fisher, Shanghai, China). The fluorescence was measured at emission (Em) wavelengths of 470 nm and 610 nm with excitation (Ex) wavelength of 370 nm using a SpectraMax i3 microplate reader (Molecular Devices, USA).

2.3 Expression and purification of Nb-CC4-ALP fusion protein

The biopanning of library and preparation of purified Nb-CC4-ALP fusion protein were described in our previous work (Zhang et al., 2018) except for using pET22b-ALP as the fusion expression vector (see Supporting Information). The Nb-CC4 sequence was amplified from Nb-CC4-pComb3xss by forward primer and reverse primer for vector construction (Table S1).

2.4 Development of anti-1-NAP ELISA

To compare the sensitivity of RFIA, TMB- and pNPP-based ELISAs were also developed, and the details are summarized in the Supporting Information.

2.5 Synthesis of AuNCs and BSA@AuNCs

The AuNCs were prepared by one-pot synthesis (Qu et al., 2019; Xue et al., 2019). Briefly, 1 mL of $HAuCl_4{\cdot}4H_2O$ solution (25 mM) was added to 8.7 mL H_2O dropwise at stirring. Then, 0.3 mL of GSH solution (100 mM) was added and rose to 70 °C for a 24 h reaction. The synthesized AuNCs were stored at 4 °C. The synthesis of BSA@AuNCs was summarized in Supporting Information.

2.6 Synthesis of SiNP-AuNC

The synthesis route of SiNPs was described by Qu et al. (2019). One millilitre of 3-aminopropyltriethoxysilane was mixed with 4 mL of H_2O and stirred at 40 °C for 10 min, and then 1.25 mL of AA (100 mM) was subsequently added. The SiNPs were finally obtained after another 20 min reaction at room temperature. SiNP-AuNC hybrid probe was synthesized by simple mixing with SiNPs and AuNCs solution.

2.7 Synthesis of MnO_2 nanosheet

The MnO_2 nanosheet was synthesized according to Yan et al. (2018). Briefly, 32 mL of sodium dodecyl sulfate (0.1 M) and 1.5 mL of H_2SO_4 were mixed and stirred at 95 °C for 15 min. Three millilitres of $KMnO_4$ (0.05 M), and 263.5 mL of H_2O was added to the mixture for another 2 h reaction to yield dark brown precipitates. The product was washed with H_2O and ethyl alcohol for three times. Finally, the obtained MnO_2 nanosheet was dispersed within an ultrasonic bath for 30 min and stored at 4 °C.

2.8 Detection of ALP

The premixed SAM solution was employed to verify the high-sensitivity response of ALP. The parameters were optimized, including the ratio of SiNPs and AuNCs, AAP concentration, MnO_2 concentration, pH value of Tris buffer for reaction, and reaction time.

2.9 Development of RFIA

To develop RFIA, Tris-HCl (5 mM, pH 7.5) was employed as the working buffer rather than PBS to avoid the inhibition of ALP by PO_4^{3-}. A series of concentrations of 1-NAP was added to antigen-coated black opaque 96-well plates (50 μL/well), and diluted Nb-CC4 was subsequently added (50 μL/well) for 40 min incubation at 37 °C. After incubation, the plate was washed five times with washing buffer (Tris-HCl with 0.05% Tween-20). Then AAP (5 mM) was added (100 μL/well) for 40 min incubation at 37 °C. For the fluorescence response, 50 μL of MnO_2 (0.1 mg/mL) was added for 10 min incubation in a shaker (37 °C, 500 rpm), whereafter 50 μL of probe solution containing SiNPs (6 μL) and AuNCs (24 μL) was added for another 10 min incubation. The fluorescence intensity was measured at wavelengths Em of 470 nm (I_{470}) and 610 nm (I_{610}) with an Ex of 370 nm. The value of I_{610}/I_{470} against the serial concentration of 1-NAP calibration curve was generated using OriginPro 8.5 software (OriginLab Corp., Northampton, MA, USA).

2.10 Recovery Test

For RFIA, spiked urine samples were diluted (20-fold) with Tris-HCl buffer. The accuracy of RFIA was validated by high-performance liquid chromatography with fluorescence detection (HPLC-FLD). The HPLC system consisted of a Shimadzu LC-20AT system equipped with a Shimadzu RF-20A fluorescence detector. C_{18} chromatographic column (XBridge™, 150 mm × 4.6 I.D., 5 μm, Waters Co. Ltd., Ireland) was used for chromatographic separation. The injection volume was 40 μL, and the flow rate was 1.2 mL/min at 35 °C. The Ex was 228 nm and measured at 425 nm. A C_{18} SPE column was employed for spiked urine sample purification. Briefly, the activation of C_{18} SPE columns were firstly rinsed by 9 mL methanol and 0.01 M HCl, respectively. The pH of urine samples (10 mL) was adjusted to 1~2 by HCl. The flow speed of samples was 2~3 mL/min. The analyte was eluted with 10 mL of methanol and filtered through a 0.22 μm membrane before HPLC-FLD analysis.

3. Results and discussion

3.1 Production and characterization of anti-1-NAP antibody

After the 3rd immunization, the characteristics of camelid antiserum was studied and results are shown in Table S2. Slight differences were observed for the inhibition using hapten 1-BSA and hapten 2-BSA (Fig. S1), whereas the titer performed by hapten 1-BSA was higher than that of hapten 2-BSA. Hence, hapten 1-BSA was chosen for the following study. The titers of antiserum from the 3rd to 6th immunizations showed no noticeable improvement (Fig. 1A). The inhibition of free 1-NAP to antiserum increased from the 3rd to 5th immunizations, and then reduced at the 6th immunization (Fig. 1B). Camelid IgG_2 and IgG_3 from 5th immunization were separated successfully (Fig. 1C) and showed good affinity for free 1-NAP (Fig. 1D), indicating that heavy chain antibodies were successfully generated. Consequently, blood from the 5th immunization was chosen for Nb isolation.

Total RNA was extracted from isolated blood lymphocytes (Fig. S2A) for cDNA synthesis. After two rounds of nested-PCR, Nb sequences were amplified successfully (Fig. S3B) and further used for phage-display library construction. Six clones, Nb-CB4, Nb-CC3, Nb-KC2,

Nb-CB3, Nb-KC4, and Nb-CC4, were obtained after three rounds of panning (Fig. S3A) and further assessed using phage ELISA. Nb-CC4 showed the highest sensitivity among these six clones and was chosen for the following experiments (Fig. S3B).

It was a challenge for the preparation of Nbs against small molecules with high affinity, especially for 1-NAP with ultra-low molecular weight (Mw:144). Rational design of hapten is the key role for the generation of Nbs and determines the sensitivity. Previously, we synthesised several novel haptens to obtain anti-1-NAP mAb and further used them for Nbs preparation in this study. After three rounds of careful biopanning from camelid phage display library and strict ELSIA test, novel Nb-CC4 was screened out. The Nb-CC4 showed affinity of 1.88×10^{13} L/mol (Fig. S3C), which was extremely higher than that of anti-1-NAP mAb (Chen et al., 2020). Moreover, in comparison with the anti-1-NAP mAb (Table 1), sensitivity improvement was observed for Nb-CC4. In general, the obtained Nb-CC4 was promising to replace conventional mAb for the analysis of 1-NAP. In subsequent study, bifunctional fusion protein, Nb-CC4-ALP, was prepared based on elaborate design, including vector construction and primer design.

3.2 Production and characterization of bifunctional Nb-CC4-ALP fusion protein

The tracers are always prepared by conjugating pesticides or their derivatives with HRP through chemical synthesis, which showed the drawbacks of complex procedures, prolonged reaction periods, significant batch errors, and high costs. Nb can overcome these shortcomings by fusing with ALP to form a bifunctional fusion protein (Nb-CC4-ALP). The SDS-PAGE and western blot confirmed the successful preparation of Nb-CC4-ALP (Fig. S4). To investigate the sensitivity of Nb-CC4-ALP, the pNPP-based one-step ELISA was developed and the result was compared with TMB-based two-step ELISA (Table 1). Interestingly, the pNPP-based ELISA showed a lower LOD and broader linear range than that of TMB-based ELISA using Nb-CC4. In general, the activity of ALP to pNPP (Faure et al., 2014; Xu et al., 2006) was lower than that of HRP to TMB (Zhang et al., 2015). Due to the lower catalytic activity, the concentration of ALP significantly affected the signal generation. Consequently, slight inhibition to Nb-CC4-ALP can cause a detectable signal decreasing. On the other hand, the pNPP-based one-step assay can better exhibit a continuous signal change with various concentration of 1-NAP owing to the equal ratio between Nb-CC4 and ALP. In contrast, TMB-based ELISA required two-step incubation, which is hard to control the molecular ratio of such binding between primary antibody (Nb-CC4) and secondary antibodies (Wang et al., 2019). As a result, calibration curve of TMB-based ELISA was narrow than that of pNPP-based ELISA, which agreed with our previous study (Zhang et al., 2018).

3.3 Construction of SAM system

Based on the good features of bifunctional fusion protein described above, we further developed a dual-emission based RFIA with the aid of SAM system (Fig.2). The SiNPs were used as an internal reference and used for AIEE of AuNCs. In the presence of the MnO_2 nanosheet, Em of SiNP-AuNC at 610 nm was quenched. The AA produced by Nb-CC4-ALP can etched the MnO_2 nanosheet and thereby recovered the fluorescence of SiNP-AuNC at 610 nm. Therefore, fluorescence signal of SAM system can be regulated

by Nb-CC4-ALP. To achieve the response mechanism described above, SAM nanomaterials were synthesized and further characterized.

3.3.1 Construction of SiNP-AuNC hybrid probe—To constructed the SAM system, fluorescent probe AuNCs and SiNPs were synthesized and characterized (Fig. 3). The transmission electron microscopy (TEM) showed spherical particles of ~3 nm for AuNCs, indicating good dispersibility (Fig. 3A). The fluorescence scanning test of AuNCs indicated the optimized Ex and Em were 370 nm and 610 nm, respectively (Fig. 3B). The survey XPS spectrum of AuNCs clearly showed the binding energy peak of Au 4*f*, S 2*p*, C 1 s, N 1*s*, and O 1*s*, which were the main elements of AuNCs (Fig. 3C).The Fourier transform infrared (FTIR) spectroscopy showed the S-H bond of GSH at stretching vibration peak of 2555.2 cm^{-1} whereas no corresponding peak was observed for AuNCs (Fig. 3D). These results indicated the GSH has participated in the reaction to form Au-S bond and the AuNCs was successful synthesized (Qu et al., 2019; Zhang et al., 2013).

To achieve AIEE of AuNCs, SiNPs was prepared by simple one-pot synthesis. The TEM image showed the uniform small size of ~2.8 nm for SiNPs (Fig. 3E). The SiNPs showed an optimal Em at 470 nm with Ex at 370 nm (Fig. 3F), which was the same as that of AuNCs and was suitable to construct dual-emission hybrid probe. The FTIR spectrum of SiNPs (Fig. 3G) showed stretching vibrations of O-H and Si-O-Si bonds at 2931 cm^{-1} and 1066 cm^{-1}, respectively. Bending vibrations and stretching of N-H bonds at 1567 cm^{-1} and 3340 cm^{-1} were observed, indicating existence of amino groups. All the above FTIR peaks confirmed the successful synthesis of SiNPs.

The zeta potential was employed to investigate the feasibility of self-assembly between SiNPs and AuNCs. As shown in Fig. 3H, obvious zeta-potential difference between negative AuNCs (−10.65 mV) and positive SiNPs (0.94 mV) was observed. Hence, the SiNP-AuNC hybrid probe can be generated through electrostatic attraction and the zeta potential of SiNP-AuNC (−6.09 mV) further confirmed the successful generation. In addition, although aggregation of AuNCs also can be triggered through other positive compounds such as metal cation (Hou et al., 2018; Liu et al., 2021; Pan et al., 2021) or peptide (You and Tseng, 2019), SiNPs was more suitable owing to the constant emission which can be used as self-calibration or internal reference.

The constructed SiNP-AuNC hybrid probe showed dual-emission with optimized Ex at 370 nm (Fig. $4A_1$). In comparison with AuNCs, the intensity at 610 nm was improvement (Fig. $4A_2$), implied the successful AIEE of AuNCs triggered by electrostatic-driven self-assembly, which is a simple and convenient strategy for fluorescence enhancement. TEM image showed that the spherical shape of SiNP-AuNC has a large size of ~330 nm (Fig. $4B_1$). The large and uniform spherical shape of SiNP-AuNC was mainly attributed to the homogeneous self-assembly between AuNCs and SiNPs. The high-angle annular dark-field (HAADF) image (Fig. $4B_2$) further confirmed a clear shape of generated SiNP-AuNC hybrid probe. Moreover, obvious aggregation of Au, Si, and O element was found from the map of energy dispersive spectroscopy (Fig. $4B_3$ and $4B_4$), confirming the self-assembly of SiNPs and AuNCs.

3.3.2 Quenching mechanism of SiNP-AuNC hybrid probe—MnO_2 nanosheet was synthesized to quench SiNP-AuNC. The TEM shows a creased and thin layer with a large size (>600 nm) of MnO_2 (Fig. 5A). Owing to the good hydrophilicity, MnO_2 nanosheets can be dispersed equably in aqueous solution and showed deep brown colour with the absorbance at 370 nm (Fig. 5B). The absorbance of the synthesized MnO_2 overlapped the Ex of SiNP-AuNC, thereby might result in inner-filter effect to quench SiNP-AuNC. However, Fig. 5C showed that only the Em of AuNCs (610 nm) can be quenched by low concentration of MnO_2 (0.1 mg/mL). In contrast, both SiNPs and SiNP-AuNC remained constant Em at 470 nm in the presence of MnO_2. We further increased the MnO_2 concentration and the fluorescence of SiNPs was finally quenched with 1 mg/mL of MnO_2 (Fig. S5), suggested that SiNPs can be quenched by high concentration of MnO_2 through inner-filter effect. However, it was confused that the complete quenching of SiNPs required more MnO_2 than that of AuNCs. Consequently, TEM was used to characterize the SiNP-AuNC-MnO_2 mixture for the studying of quenching mechanism. Fig. 5D showed that the MnO_2 nanosheet partly covered on the surface of the SiNP-AuNC sphere, while no apparent alteration was observed for the SiNP-AuNC. The low concentration of MnO_2 resulted in the localized coverage, which was too insufficient to result in inner-filter effect or Förster resonance energy transfer. Therefore, we reasoned that there must be a paramount mechanism to control the quenching of AuNCs.

The Au-S bond formed by glutathione was the main capping and protection group to stabilized the structure of AuNCs (Kang and Kim, 2020; Pan et al., 2021). As a nanozyme, MnO_2 with powerful oxidase-mimic activity (Chi et al., 2019; Xiao et al., 2020) can easily break the Au-S bond and thereby quenched the fluorescence. The fluorescence recovery test was processed and the results showed that when AuNCs was premixed with MnO_2, no fluorescence recovery was observed after adding AA (Fig. S6), which didn't agree with some previous reports (Sheng et al., 2018; Zeng et al., 2018). Different from this study, these previous reports used BSA as capping reagent to synthesize AuNCs (BSA@AuNCs), which formed a protective layer to prevent gold core and Au-S bond from oxidation by MnO_2. To confirmed the above inference, the BSA@AuNCs was also synthesized and employed for fluorescence recovery test. The results showed that no apparent quenching after mixing BSA@AuNCs with MnO_2 (Fig. S7). Furthermore, we employed high-resolution XPS spectra to characterize the SiNP-AuNC-MnO_2 mixture and found that the Au $4f_{7/2}$ peak of the AuNCs shifted from 84.36 eV (Au^0) to 84.51 eV (Au^{3+}). The slight shift demonstrated the Au-S bond was broken owing to the strong oxidative activity of MnO_2 and thereby quenched the emission (Hu et al., 2016b; Qu et al., 2019). These results clearly indicated that oxidation of MnO_2 was the main reason for the quenching of AuNCs.

3.4 Optimization of SAM system to response AA

AAP is the substrate of ALP for the generation of AA, which is a powerful reductant and has been reported with extremely activity to etch MnO_2 (Wang et al., 2021; Yang et al., 2020). Since MnO_2 was the key controller for the quenching of SiNP-AuNC hybrid probe, the constructed SAM system can be consequently utilized for ALP analysis.

To achieve the highest sensitivity for ALP, several parameters of the SAM system were optimized. Fig 6A showed that the I_{610} decreased as the percentage of SiNPs increased, which can be explained that the excess SiNPs covered on AuNCs and thereby reduce the I_{610}. The highest fluorescence signal was achieved with SiNPs:AuNCs at a ratio of 1:4, which was chose as optimized parameter. Fig. 6B showed that the I_{610} reached to the highest level with an AAP concentration of 5 mM and subsequently decreased as the increasing AAP. The excess AAP might result in the high level of PO_4^{3-} and thereby inhibit the activity of ALP (Liu and Liu, 2020). The completely quenching was achieved with a MnO_2 concentration of 0.1 mg/mL (Fig. 6C). The optimized pH value and reaction time of ALP were 9.5 and 40 min, respectively (Fig. 6D and E). Finally, the constructed SAM system was applied to detect ALP with optimized parameters, and an obvious signal response was achieved with just 0.064 mU (Fig. 6F), which can be employed for the subsequent high-sensitivity RFIA development.

3.5 Development of Nb-CC4-ALP fusion protein-based RFIA

Sensitive analysis of 1-NAP was a promising approach to monitor the exposure of carbaryl. We previous reported an anti-1-NAP sensitive mAb for the detection of 1-NAP (Chen et al., 2020). Nevertheless, the sensitivity of the reported mAb was limited by matrix effect of urine samples. Fortunately, the high stability of Nbs inspired us to propose a Nb-based immunoassay to overcome the limitation of matrix effect. Finally, Nb-CC4 was finally prepared to develop sensitive immunoassay. However, it was unexpected that obvious matrix effect was still observed in icELISA test and limited the binding activity of Nb-CC4, which also required 20-fold dilution to remove matrix effect (Fig. S8). Therefore, we further constructed the SAM system and Nb-CC4-ALP bifunctional fusion protein to put forward a RFIA in order to improve sensitivity.

The titer response test showed that of RFIA exhibited a higher signal response than that of pNPP-base ELISA with just 0.16 μg/mL of Nb-CC4-ALP (Fig. 7A). The remarkable response was ascribed to the efficient chain regulation of AA-MnO_2-AuNCs. Attributed to the powerful reducing capacity, AA showed ultra-efficiency to etch MnO_2 for fluorescence recovery. In this regulation chain, MnO_2 was the connector to the control of fluorescent signal of AuNCs by AA. Hence, detectable fluorescent signal response can be achieved by low concentration of Nb-CC4-ALP, which explained the higher titer by using RFIA.

With optimal coating concentration (Table S3), a RFIA calibration curve against 1-NAP was finally obtained (Fig. 7B). This method showed a high sensitivity (IC_{50}) of 1.8 ng/mL with an LOD of 0.01 ng/mL and a linear range from 0.05 to 66.35 ng/mL. Compared with the pAb-based ELISA and mAb-based ELSIA, the developed RFIA exhibited 1000-fold and 220-fold sensitivity (IC_{50}) improvement, respectively (Table 1). Moreover, the pretreatment procedure of RFIA only required approximately 5~10 mins, which was extremely convenient and efficient than that of instrument methods (40~60 mins). Although the sensitivity of RFIA reduced by 20-fold dilution for sample analysis, the LOD (0.2 ng/mL) was still obvious lower than that of other methods. The proposed RFIA mainly overcame the shortcoming of insufficient sensitivity of rapid detection for 1-NAP. Moreover, the assay showed advantage of high-throughput in compared with chromatographic analysis.

For example, 24~32 samples can be screened with approximately 90 mins by using RFIA, while HPLC-FLD required at least approximately 192~256 mins (Fig. S9). Furthermore, 1-NAP was excreted in urine within 24 hours, which required a long period for sample collection (e.g., 3~5 days) in order to better screen out positive samples. As a result, the number of samples will be substantially increased, which further limit the application of instrument methods for 1-NAP monitoring. On the other hand, although other sensors (Bartilotti et al., 2021; Qin and Yan, 2018) were rapider than RFIA for single sample analysis, the RFIA exhibited the advantage of higher sensitivity and high-throughput, which was more suitable for the regional mass screening in key area (e.g., countryside) and providing timely results due to the high efficiency for detection.

3.6 Specificity test

Nine analogues were further employed to evaluate specificity of Nb-CC4-ALP and their structures are summarized in Fig. S10. Negligible cross-reactivity (CR) was observed for these analogues, indicating the high specificity of Nb-CC4-ALP (Fig. 7C). To be noticed, although the chemical structure of 2-NAP was the most similar to 1-NAP, no apparent CR was observed. There might be some obstructive factors on the position 2 of naphthalene nucleus, such as hydrophobic interaction, charge repulsion, or steric hindrance, as well as the other naphthol analogues. For carbaryl, the low CR might be mainly caused by the steric hindrance of the carbamate group, which leaded to the low binding affinity of the Nb-CC4-ALP to carbaryl. In the future work, the three-dimensional model of Nb-CC4 will be created from homologous modelling or protein crystal to study the immune recognition mechanism and the directed evolution.

3.7 Anti-interference test of RFIA

To assess the anti-interference ability of RFIA, the background signal was measured and compared with other mono signal methods (Table 2). The titer of TMB or pNPP-based ELISA was measured at the absorbance of 405 nm and 450 nm, respectively. Relatively, titer of RFIA was generated from the value of I_{610}/I_{470}. To further quantize and characterize the anti-interference ability, the coefficient of variation (CV) was calculated and used as an evaluation index. The RFIA showed the lowest CV value amount of these three methods, indicating good signal stability and low background noise of RFIA. Two main reasons can explain the excellent anti-interference ability of RFIA: (1) The AIEE improve the fluorescent signal of AuNCs and further attribute the high sensitivity of fluorescence analysis (Yi et al., 2020); (2) The SiNPs was introduced as internal reference to achieve self-calibration of dual emission of RFIA, which have advantage of anti-background interference to avoid influence of background noise (Guo et al., 2021; Zhang et al., 2021).

3.8 Analysis of urine sample by RFIA

To evaluated the accuracy and practicability of RFIA, recovery test was performed. Six levels of 1-NAP (20, 200, 400, 600, 800, and 1000 ng/mL) were spiked into blank urine samples and subsequently diluted 20-fold by Tris-HCl (5 mM, pH 7.4). The average recoveries are summarized in Table S4. The results showed a desirable range from 80.1% to 119.8% by RFIA, with CVs ranging between 4.4%~14.1%. The HPLC-FLD was employed to validate the accuracy of RFIA and the results showed average recoveries ranging from

71.7% to 104.6% with CVs from 1.4% to 9.8%. The results of RFIA showed good agreement and correlation with HPLC-FLD (Fig. 7D), indicating desirable accuracy and reliability of the developed RFIA, which was suitable to detect 1-NAP in urine samples with high sensitivity.

To further confirm the screening ability of the proposed RFIA, twelve blind urine samples from volunteers from Guangzhou city were determined and validated by HPLC-FLD. All the samples were free of 1-NAP. To further confirm the reliability and practicability of RFIA, the twelve samples were further spiked with several concentrations of 1-NAP randomly, and were determined by both RFIA and HPLC-FLD. The proposed RFIA was able to screen out of positive samples with good recovery (Table S5), demonstrating great promise as a tool for rapid screening of 1-NAP.

Although excellent sensitivity was achieved, the proposed RFIA still required at least approximately 90 min due to the long incubation time for catalysis and the multistep signal generation, which limited the advantages of the rapidness of the one-step strategy. Moreover, the requirement of microplate washer and reader limited the application of on-site tests. More rapid and efficient methods should be developed to overcome these drawbacks, mobile biosensors such as lateral flow immunoassays or mobile electrochemical immunosensors were potential tools for 1-NAP analysis in the following work.

4. Conclusions

In this study, we selected several nanobodies specific for the biomarker 1-NAP of carbaryl. The optimal nanobody with good characteristics was then fused with alkaline phosphatase to form a bifunctional reagent. By the aid of several nanomaterials, silicon nanoparticles (SiNPs), nanoclusters (AuNCs) and MnO_2 nanosheet, a dual-emission system based ratiometric fluoroimmunoassay (RFIA) with good sensitivity, rapidity, high throughput, and low cost was developed for 1-NAP. In comparison with conventional monoclonal or polyclonal antibody-based ELISA, the proposed assay showed significant improvement on assay sensitivity. In stead of chemical synthesis, generic fusion technique was used to prepare the immunosensor tracer, which greatly improved the batch errors. The results of recovery test obtained by the proposed assay and the standard HPLC-FLD showed good consistence. The results of this work proved a platform for the quick and sensitive screening of hazardous materials in agricultural and environmental samples.

Supplementary Material

Refer to Web version on PubMed Central for supplementary material.

Acknowledgments

This work was supported by the National Key Research and Development of China (2018YFC1602904), the Science and Technology Foundation of Guangdong Province (2018A050506072), the Key Project of Guangdong Provincial High School (2019KJDXM002), the National Institutes of Environmental Health Sciences Superfund Research Program (P42ES04699) and the NIEHS RIVER Award (R35 ES030443-01).

References

Aprea C, Colosio C, Mammone T, Minoia C, Maroni M, 2002. Biological monitoring of pesticide exposure: a review of analytical methods. J. Chromatogr. B 769, 191–219.

Arcury TA, Quandt SA, Barr DB, Hoppin JA, McCauley L, Grzywacz JG, Robson MG, 2006. Farmworker exposure to pesticides: methodologic issues for the collection of comparable data. Environ. Health Persp 114, 923–928.

Bartilotti M, Beluomini MA, Boldrin Zanoni MV, 2021. Using an electrochemical MIP sensor for selective determination of 1-naphthol in oilfield produced water. Electroanal. 33, 1346–1355.

Berman T, Goeen T, Novack L, Beacher L, Grinshpan L, Segev D, Tordjman K, 2016. Urinary concentrations of organophosphate and carbamate pesticides in residents of a vegetarian community. Environ. Int 96, 34–40. [PubMed: 27588700]

Bever CS, Dong JX, Vasylieva N, Barnych B, Cui Y, Xu ZL, Hammock BD, Gee SJ, 2016. VHH antibodies: emerging reagents for the analysis of environmental chemicals. Anal. Bioanal. Chem 408, 5985–6002. [PubMed: 27209591]

Bonvallot N, Jamin EL, Regnaut L, Chevrier C, Martin J, Mercier F, Cordier S, Cravedi J, Debrauwer L, Le Bot B, 2021. Suspect screening and targeted analyses: two complementary approaches to characterize human exposure to pesticides. Sci. Total Environ 786, 147499.

Bravo R, Caltabiano LM, Fernandez C, Smith KD, Gallegos M, Whitehead RD, Weerasekera G, Restrepo P, Bishop AM, Perez JJ, Needham LL, Barr DB, 2005. Quantification of phenolic metabolites of environmental chemicals in human urine using gas chromatography-tandem mass spectrometry and isotope dilution quantification. J. Chromatogr. B 820, 229–236.

Chen ZJ, Liu XX, Xiao ZL, Fu HJ, Huang YP, Huang SY, Shen YD, He F, Yang XX, Hammock B, Xu ZL, 2020. Production of a specific monoclonal antibody for 1-naphthol based on novel hapten strategy and development of an easy-to-use ELISA in urine samples. Ecotox. Environ. Safe 196, 110533.

Chi MQ, Zhu Y, Jing LW, Wang C, Lu XF, 2019. Fabrication of oxidase-like polyaniline-MnO_2 hybrid nanowires and their sensitive colorimetric detection of sulfite and ascorbic acid. Talanta 191, 171–179. [PubMed: 30262047]

Didpinrum P, Ponhong K, Siriangkhawut W, Supharoek S, Grudpan K, 2020. A cost-effective spectrophotometric method based on enzymatic analysis of jackfruit latex peroxidase for the determination of carbaryl and its metabolite 1-napthol residues in organic and chemical-free vegetables. Food Anal. Method 13, 433–444.

Esteve-Romero J, Marco-Peiro S, Rambla-Alegre M, Durgbanshi A, Bose D, Mourya SK, 2012. A micellar liquid chromatographic method for the determination of carbaryl and 1-naphthol in biological samples. J. Liq. Chromatogr. R. T 35, 355–361.

Faure M, Sotta B, Gamby J, 2014. Investigating the kinetics of paramagnetic-beads linked alkaline phosphatase enzyme through microchannel resistance measurement in dielectric microchip. Biosens. Bioelectron 58, 61–67. [PubMed: 24613971]

Freire C, Suárez B, Vela-Soria F, Castiello F, Reina-Pérez I, Andersen HR, Olea N, Fernández MF, 2021. Urinary metabolites of non-persistent pesticides and serum hormones in Spanish adolescent males. Environ. Res 197, 111016. [PubMed: 33771511]

Fu HJ, Chen ZJ, Wang H, Luo L, Wang Y, Huang RM, Xu ZL, Hammock B, 2021. Development of a sensitive non-competitive immunoassay via immunocomplex binding peptide for the determination of ethyl carbamate in wine samples. J. Hazard. Mater 406, 124288. [PubMed: 33525128]

Gaudreau E, Berube R, Bienvenu J, Fleury N, 2016. Stability issues in the determination of 19 urinary (free and conjugated) monohydroxy polycyclic aromatic hydrocarbons. Anal. Bioanal. Chem 408, 4021–4033. [PubMed: 27098935]

Guo JQ, Liu AK, Zeng YT, Cai HJ, Ye S, Li H, Yan W, Zhou FF, Song J, Qu JL, 2021. Noval dual-emission fluorescence carbon dots as a ratiometric probe for Cu^{2+} and ClO^{-} detection. Nanomaterials 11, 1232. [PubMed: 34067118]

Hemmateenejad B, Shahrivar-Kevishahi A, Shakerizadeh-Shirazi F, 2016. Reversible photobleaching of gold nanoclusters: a mechanistic investigation. J. Phys. Chem. C 120, 28215–28223.

Hou WL, Chen Y, Lu QJ, Liu ML, Zhang YY, Yao SZ, 2018. Silver ions enhanced AuNCs fluorescence as a turn-off nanoprobe for ultrasensitive detection of iodide. Talanta 180, 144–149. [PubMed: 29332792]

Hu Y, Chiu YH, Hauser R, Chavarro J, Sun Q, 2016a. Overall and class-specific scores of pesticide residues from fruits and vegetables as a tool to rank intake of pesticide residues in United States: a validation study. Environ. Int 92-93, 294–300. [PubMed: 27128714]

Hu XL, Wu XM, Fang X, Li ZJ, Wang GL, 2016b. Switchable fluorescence of gold nanoclusters for probing the activity of alkaline phosphatase and its application in immunoassay. Biosens. Bioelectron 77, 666–672. [PubMed: 26496220]

Hua XD, Ding Y, Yang JC, Ma M, Shi HY, Wang MH, 2017. Direct competitive fluoroimmunoassays for detection of imidaclothiz in environmental and agricultural samples using quantum dots and europium as labels. Sci. Total Environ 583, 222–227. [PubMed: 28117157]

Jacobson MH, Wu Y, Liu M, Kannan K, Li AJ, Robinson M, Warady BA, Furth S, Trachtman H, Trasande L, 2021. Organophosphate pesticides and progression of chronic kidney disease among children: a prospective cohort study. Environ. Int 155, 106597. [PubMed: 33951537]

Jain V, Bhagat S, Singh S, 2021. Bovine serum albumin decorated gold nanoclusters: a fluorescence-based nanoprobe for detection of intracellular hydrogen peroxide. Sensor. Actuat. B 327, 128886.

Ji HW, Wu L, Pu F, Ren JS, Qu XG, 2018. Point-of-care identification of bacteria using protein-encapsulated gold nanoclusters. Adv. Healthcare Mater 7, 1701370.

Jin M, Mou ZL, Zhang RL, Liang SS, Zhang ZQ, 2017. An efficient ratiometric fluorescence sensor based on metal-organic frameworks and quantum dots for highly selective detection of 6-mercaptopurine. Biosens. Bioelectron 91, 162–168. [PubMed: 28006684]

Kang Y, Kim J, 2020. Electrochemiluminescence of glutathione-stabilized Au nanoclusters fractionated by gel electrophoresis in water. Chem. Electro. Chem 7, 1092–1096.

Kramer PM, Marco M, Hammock BD, 1994. Development of a selective enzyme-linked immunosorbent assay for 1-naphthol-the major metabolite of carbaryl (1-naphthyl N-methylcarbamate). J. Agr. Food Chem 42, 934–943.

Li C, Tang ZO, Hu ZX, Wang YW, Yang XM, Mo FZ, Lu XL, 2018. Natural single-domain antibody-nanobody: a novel concept in the antibody field. J. Biomed. Nanotechnol 14, 1–19. [PubMed: 29463363]

Liang Y, Wei L, Hu J, 2021. Residues and dietary intake risk assessments of clomazone, fomesafen, haloxyfop-methyl and its metabolite haloxyfop in spring soybean field ecosystem. Food Chem. 360, 129921. [PubMed: 33991974]

Lin XF, Tian M, Cao CC, Shu T, Wang J, Wen YQ, Su L, Zhang XJ, 2021. Strongly phosphorescent and water-soluble gold(I)-silver(I)-cysteine nanoplatelets via versatile small biomolecule cysteine-assisted synthesis for intracellular hypochlorite detection. Biosens. Bioelectron 193, 113571. [PubMed: 34425519]

Liu HY, Liu JW, 2020. Self-limited Phosphatase-mimicking CeO_2 Nanozymes. Chem. Nano. Mat 6, 947–952.

Liu YB, Zhang Y, Zhang W, Wang XH, Sun Y, Huang YB, Ma PY, Ding J, Song DQ, 2021. Ratiometric fluorescent sensor based on MoS_2 QDs and AuNCs for determination and bioimaging of alkaline phosphatase. Spectrochim. Acta A 262, 120087.

Liu YH, Mo RH, Tang FB, Fu Y, Guo YR, 2015. Influence of different formulations on chlorpyrifos behavior and risk assessment in bamboo forest of China. Environ. Sci. Pollut. R 22, 20245–20254.

Maroni M, Colosio C, Ferioli A, Fait A, 2000. Biological monitoring of pesticide exposure: a review. Toxicology 143, 1–118. [PubMed: 10675783]

Niu WJ, Shan D, Zhu RH, Deng SY, Cosnier S, Zhang XJ, 2016. Dumbbell-shaped carbon quantum dots/AuNCs nanohybrid as an efficient ratiometric fluorescent probe for sensing cadmium (II) ions and l-ascorbic acid. Carbon 96, 1034–1042.

Oates L, Cohen M, 2011. Assessing diet as a modifiable risk factor for pesticide exposure. Int. J. Env. Res. Pub. He 8, 1792–1804.

Pan TT, Zhou T, Tu YF, Yan JL, 2021. Turn-on fluorescence measurement of acid phosphatase activity through an aggregation-induced emission of thiolate-protected gold nanoclusters. Talanta 227, 122197. [PubMed: 33714471]

Peng F, Hardy EM, Mezzache S, Bourokba N, Palazzi P, Stojiljkovic N, Bastien P, Li J, Soeur J, Appenzeller BMR, 2020. Exposure to multiclass pesticides among female adult population in two Chinese cities revealed by hair analysis. Environ. Int 138, 105633. [PubMed: 32179318]

Petropoulou S, Gikas E, Tsarbopoulos A, Siskos PA, 2006. Gas chromatographic-tandem mass spectrometric method for the quantitation of carbofuran, carbaryl and their main metabolites in applicators' urine. J. Chromatogr. A 1108, 99–110. [PubMed: 16442549]

Qin SJ, Yan B, 2018. A facile indicator box based on Eu^{3+} functionalized MOF hybrid for the determination of 1-naphthol, a biomarker for carbaryl in urine. Sensor. Actuat. B 259, 125–132.

Qu F, Meng L, Zi Y, You J, 2019. Ratiometric detection of alkaline phosphatase based on aggregation-induced emission enhancement. Anal. Bioanal. Chem 411, 7431–7440. [PubMed: 31655858]

Rousis NI, Gracia-Lor E, Zuccato E, Bade R, Baz-Lomba JA, Castrignanò E, Causanilles A, Covaci A, de Voogt P, Hernàndez F, Kasprzyk-Hordern B, Kinyua J, McCall A, Plósz BG, Ramin P, Ryu Y, Thomas KV, van Nuijs A, Yang Z, Castiglioni S, 2017. Wastewater-based epidemiology to assess pan-European pesticide exposure. Water Res. 121, 270–279. [PubMed: 28554112]

Sancho JV, Cabanes RA, López FJ, Hernández F, 2003. Direct determination of 1-naphthol in human urine by coupled-column liquid chromatography with fluorescence detection. Chromatographia 58, 565–569.

Saquib Q, Siddiqui MA, Ansari SM, Alwathnani HA, Musarrat J, Al Khedhairy AA, 2021. Cytotoxicity and genotoxicity of methomyl, carbaryl, metalaxyl, and pendimethalin in human umbilical vein endothelial cells. J. Appl. Toxicol 41, 832–846. [PubMed: 33427323]

Serdar B, Waidyanatha S, Zheng Y, Rappaport SM, 2008. Simultaneous determination of urinary 1- and 2-naphthols, 3- and 9-phenanthrols, and 1-pyrenol in coke oven workers. Biomarkers 8, 93–109.

Shahdost-fard F, Fahimi-Kashani N, Hormozi-nezhad MR, 2021. A ratiometric fluorescence nanoprobe using CdTe QDs for fast detection of carbaryl insecticide in apple. Talanta 221, 121467. [PubMed: 33076086]

Sheng JP, Jiang XX, Wang LQ, Yang MH, Liu YN, 2018. Biomimetic mineralization guided one-pot preparation of gold clusters anchored two-dimensional MnO_2 nanosheets for fluorometric/magnetic bimodal sensing. Anal. Chem 90, 2926–2932. [PubMed: 29363313]

Silver M, Shao J, Chen M, Xia Y, Lozoff B, Meeker J, 2016. Distribution and predictors of pesticides in the umbilical cord blood of Chinese newborns. Int. J. Env. Res. Pub. He 13, 94.

Sinha SN, Banda VR, 2018. Correlation of pesticide exposure from dietary intake and bio-monitoring: the different sex and socio-economic study of children. Ecotox. Environ. Safe 162, 170–177.

Tian F, Zhou J, Jiao B, He Y, 2019. A nanozyme-based cascade colorimetric aptasensor for amplified detection of ochratoxin A. Nanoscale 11, 9547–9555. [PubMed: 31049533]

Wang HP, Liang YJ, Sun YJ, Hou WY, Chen JX, Long DX, Xu MY, Wu YJ, 2014. Subchronic neurotoxicity of chlorpyrifos, carbaryl, and their combination in rats. Environ. Toxicol 29, 1193–1200. [PubMed: 23418109]

Wang K, Liu ZP, Ding GC, Li J, Vasylieva N, Li QX, Li DY, Gee SJ, Hammock BD, Xu T, 2019. Development of a one-step immunoassay for triazophos using camel single-domain antibody–alkaline phosphatase fusion protein. Anal. Bioanal. Chem 411, 1287–1295. [PubMed: 30706076]

Wang RJ, Wang ZH, Rao HH, Xue X, Luo MY, Xue ZH, Lu XQ, 2021. A two fluorescent signal indicator-based ratio fluorometric alkaline phosphatase assay based on one signal precursor. Chem. Commun 57, 4444–4447.

Xiao PY, Liu Y, Zong WJ, Wang J, Wu MH, Zhan JJ, Yi XL, Liu LF, Zhou H, 2020. Highly selective colorimetric determination of catechol based on the aggregation-induced oxidase–mimic activity decrease of δ-MnO_2. RSC Adv. 10, 6801–6806.

Xu Y, Liu X, Ip MPC, 2006. Michaelis-menten analysis of alkaline phosphatase by capillary electrophoresis using plug-plug reaction. J. Liq. Chromatogr. R. T 21, 2781–2797.

Xue FF, Qu F, Han WL, Xia LA, You JM, 2019. Aggregation-induced emission enhancement of gold nanoclusters triggered by silicon nanoparticles for ratiometric detection of protamine and trypsin. Anal. Chim. Acta 1046, 170–178. [PubMed: 30482296]

Yan X, Li H, Han X, Su X, 2015. A ratiometric fluorescent quantum dots based biosensor for organophosphorus pesticides detection by inner-filter effect. Biosens. Bioelectron 74, 277–83. [PubMed: 26143468]

Yan X, Song Y, Zhu C, Li H, Du D, Su X, Lin Y, 2018. MnO_2 nanosheet-carbon dots sensing platform for sensitive detection of organophosphorus pesticides. Anal. Chem 90, 2618–2624. [PubMed: 29237266]

Yang Q, Li CY, Li JH, Arabi M, Wang XY, Peng HL, Xiong H, Choo J, Chen LX, 2020. Multi-emitting fluorescence sensor of MnO_2-OPD-QD for the multiplex and visual detection of ascorbic acid and alkaline phosphatase. J. Mater. Chem. C 8, 5554–5561.

Yi KY, Zhang XT, Zhang L, 2020. Eu^{3+}@metal–organic frameworks encapsulating carbon dots as ratiometric fluorescent probes for rapid recognition of anthrax spore biomarker. Sci. Total Environ 743, 140692. [PubMed: 32653714]

You JG, Lu CY, Krishna Kumar AS, Tseng WL, 2018. Cerium(iii)-directed assembly of glutathione-capped gold nanoclusters for sensing and imaging of alkaline phosphatase-mediated hydrolysis of adenosine triphosphate. Nanoscale 10, 17691–17698. [PubMed: 30206623]

You JG, Tseng WL, 2019. Peptide-induced aggregation of glutathione-capped gold nanoclusters: a new strategy for designing aggregation-induced enhanced emission probes. Anal. Chim. Acta 1078, 101–111. [PubMed: 31358207]

Zeng RJ, Tang Y, Zhang LJ, Luo ZB, Tang DP, 2018. Dual-readout aptasensing of antibiotic residues based on gold nanocluster-functionalized MnO_2 nanosheets with target-induced etching reaction. J. Mater. Chem. B 6, 8071–8077. [PubMed: 32254926]

Zhang HY, Liu Q, Wang T, Yun ZJ, Li GL, Liu JY, Jiang GB, 2013. Facile preparation of glutathione-stabilized gold nanoclusters for selective determination of chromium (III) and chromium (VI) in environmental water samples. Anal. Chim. Acta 770, 140–146. [PubMed: 23498696]

Zhang K, Zuo W, Wang ZY, Liu J, Li TR, Wang BD, Yang ZY, 2015. A simple route to $CoFe_2O_4$ nanoparticles with shape and size control and their tunable peroxidase-like activity. RSC Adv. 5, 10632–10640.

Zhang YQ, Xu ZL, Wang F, Cai J, Dong JX, Zhang JR, Si R, Wang CL, Wang Y, Shen YD, Sun YM, Wang H, 2018. Isolation of bactrian camel single domain antibody for parathion and development of one-step dc-FEIA method using vhh-alkaline phosphatase fusion protein. Anal. Chem 90, 12886–12892. [PubMed: 30256086]

Zhang JL, Dai X, Song ZL, Han R, Ma LZ, Fan GC, Luo XL, 2020. One-pot enzyme- and indicator-free colorimetric sensing of glucose based on MnO_2 nano-oxidizer. Sensor. Actuat. B 304, 127304.

Zhang YH, Zhou K, Qiu Y, Xia L, Xia ZN, Zhang KL, Fu QF, 2021. Strongly emissive formamide-derived N-doped carbon dots embedded Eu(III)-based metal-organic frameworks as a ratiometric fluorescent probe for ultrasensitive and visual quantitative detection of Ag^+. Sensor. Actuat. B 339, 129922.

Zhao YJ, Zheng XH, Wang QZ, Zhe TT, Bai YW, Bu T, Zhang M, Wang L, 2020. Electrochemical behavior of reduced graphene oxide/cyclodextrins sensors for ultrasensitive detection of imidacloprid in brown rice. Food Chem. 333, 127495. [PubMed: 32663747]

Zhu XC, Jiang W, Zhao Y, Liu HL, Sun BG, 2021. Single, dual and multi-emission carbon dots based optosensing for food safety. Trends. Food Sci. Tech 111, 388–404.

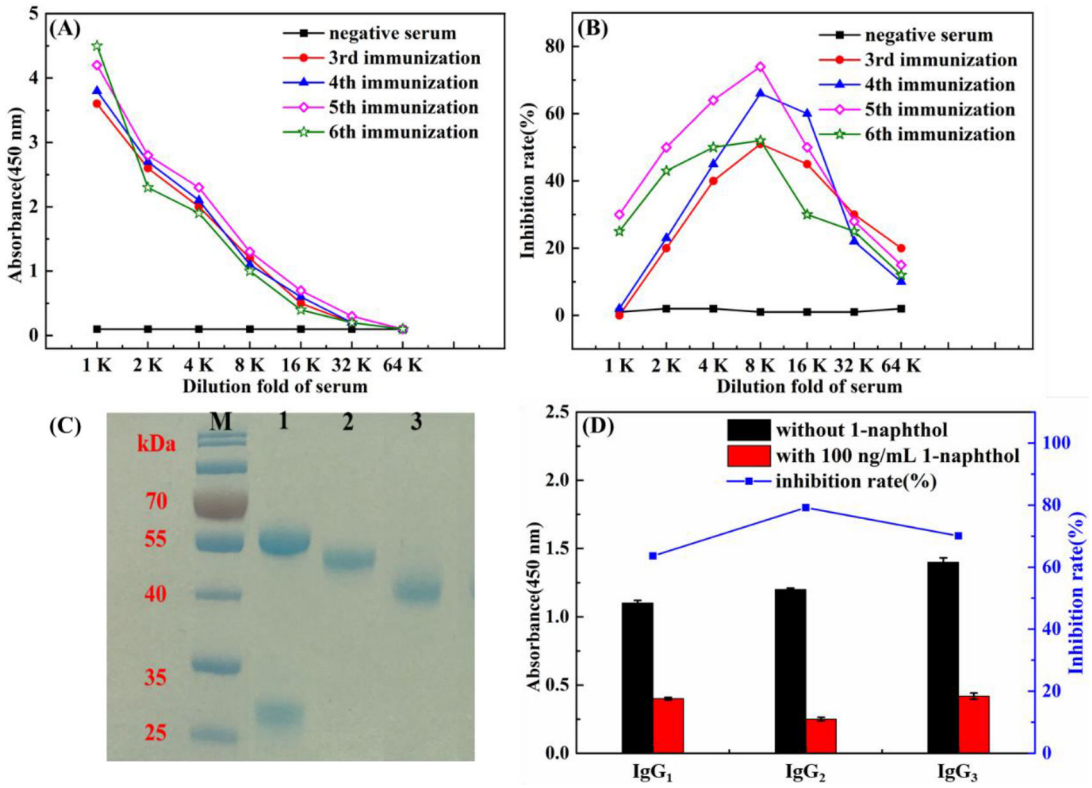

Fig. 1.

(A) The titer of camelid antiserum, hapten 1-BSA (1 μg/mL) was employed for coating antigen; (B) Inhibition of free 1-NAP (1 μg/mL) to camelid antiserum; (C) Subtype separation of camelid antibodies, M: marker, lane 1: IgG_1, lane 2: IgG_2 lane 3: IgG_3; (D) Inhibition of camelid IgG_1, IgG_2, IgG_3.

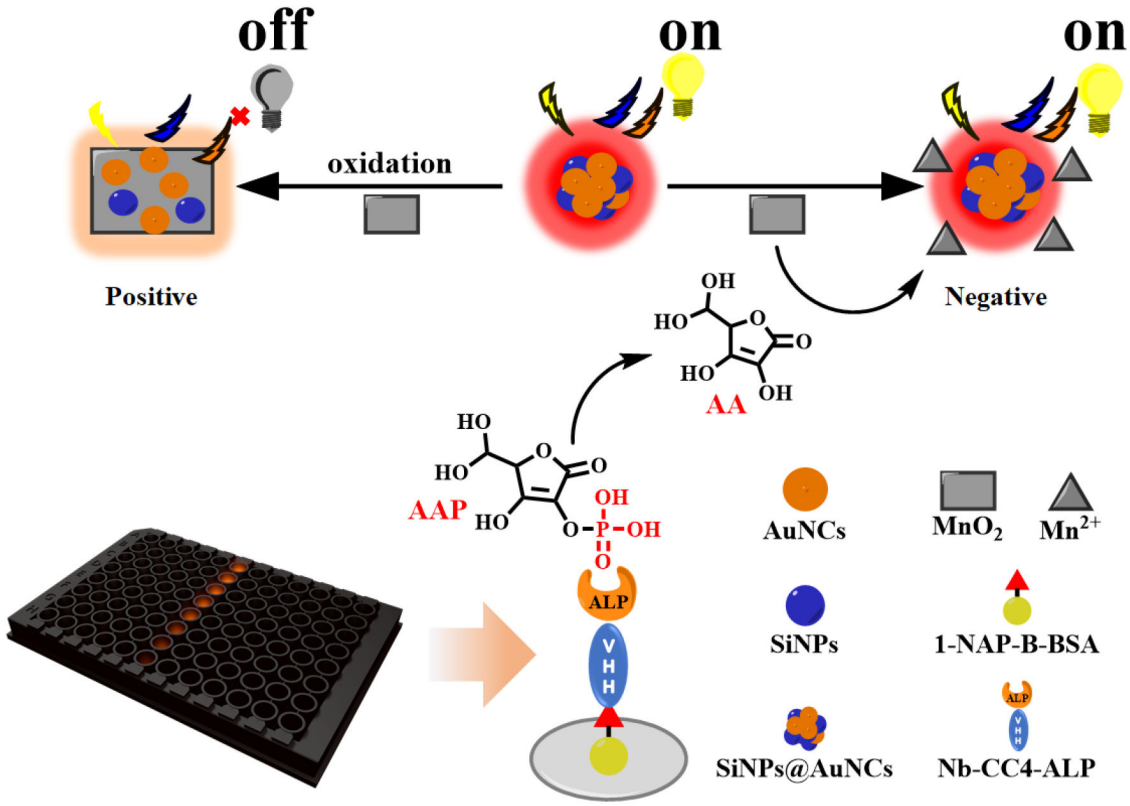

Fig. 2.

Schematic diagram of RFIA. Ascorbic acid phosphate (AAP); Ascorbic acid (AA); Alkaline phosphatase (ALP); 1-naphthol (1-NAP)

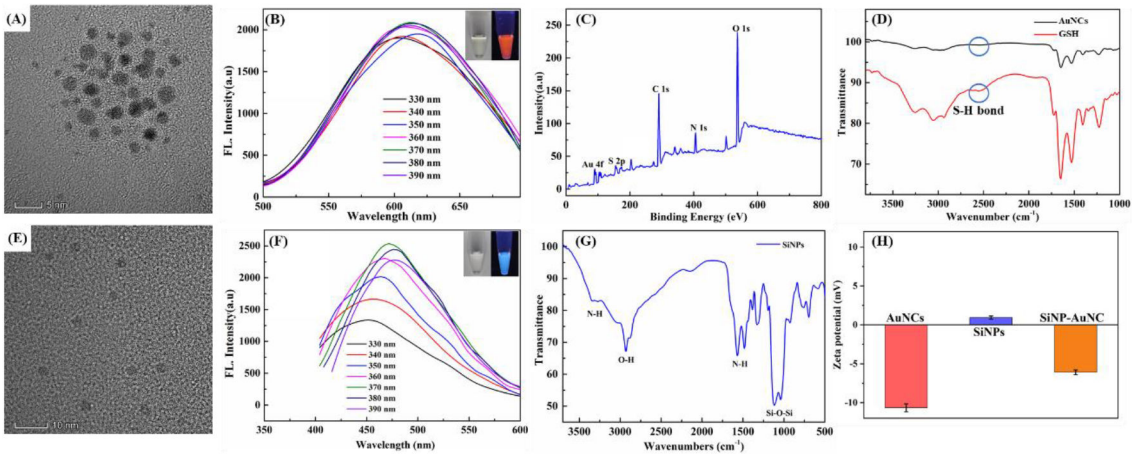

Fig. 3.

The (A)TEM image, (B) emission spectrum, (C) XPS spectrum, and (D) FTIR spectrum of AuNCs. The blue circles indicate the FT-IR spectrum peak of S-H bond. The (E)TEM image, (F) emission spectrum, and (G) FTIR spectrum of SiNPs. (H) The zeta potential of AuNCs, SiNPs, and SiNP-AuNC.

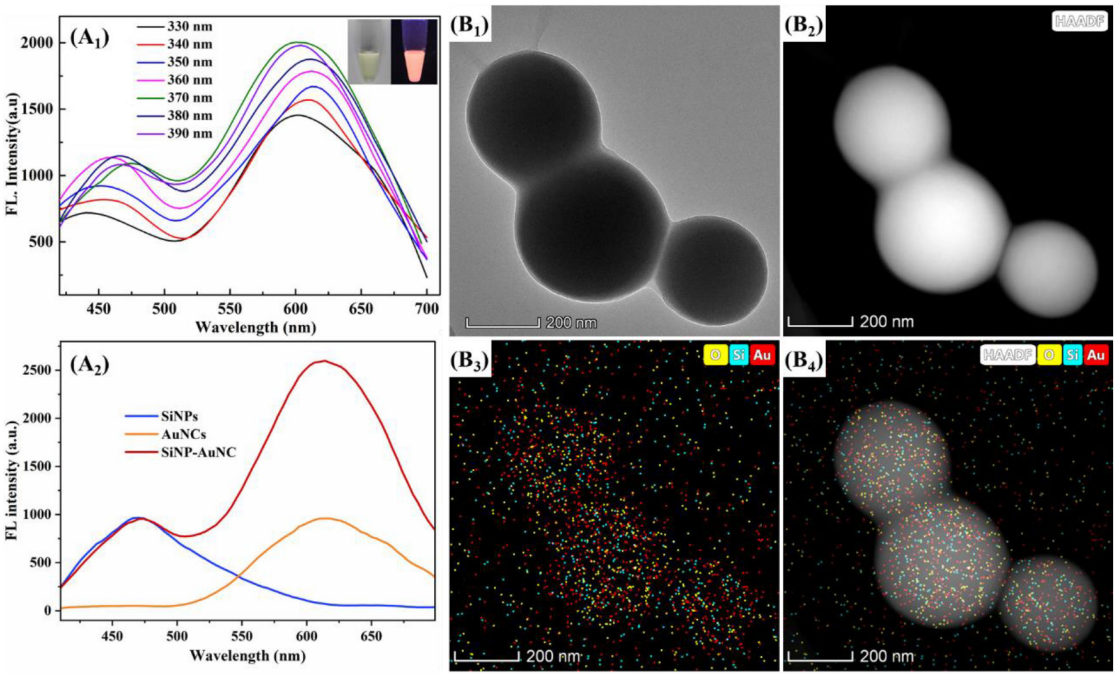

Fig. 4.

(A_1) Ex optimizing of SiNP-AuNC; (A_2) The emission spectrum of AuNCs, SiNPs, and SiNP-AuNC; (B_1) TEM image of SiNP-AuNC; The (B_2) HAADF image and (B_3 and B_4) energy dispersive spectroscopy map of SiNP-AuNC.

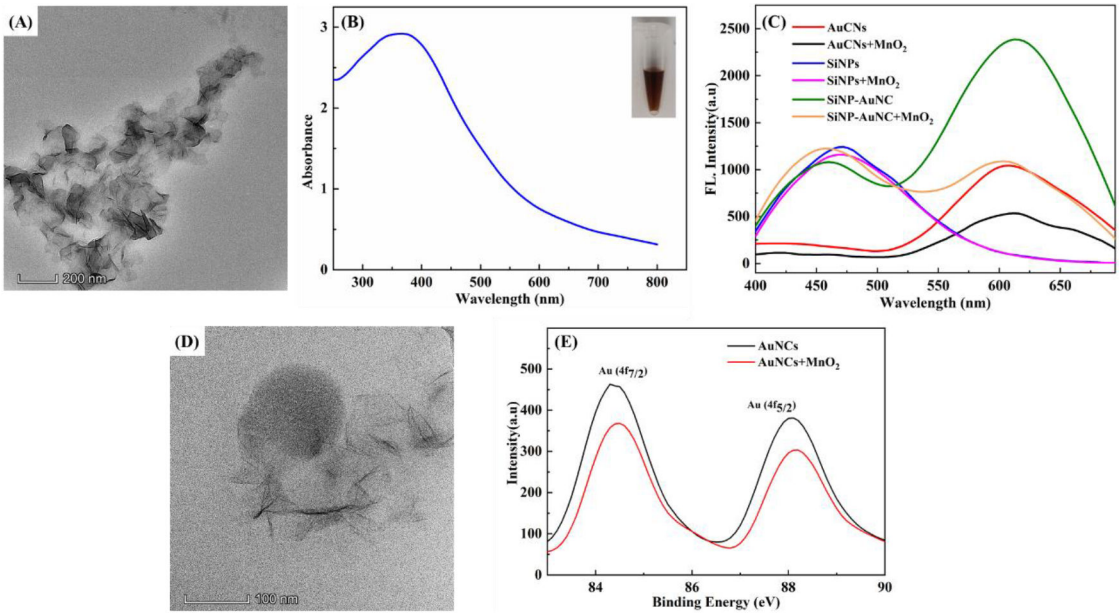

Fig. 5.

(A) The TEM image and absorbance of MnO_2 nanosheet; (B) The spectrum of SiNP-AuNC in the absence or presence of MnO_2 nanosheet; (D) TEM image of SAM mixture; (D) High resolution of Au $4f_{7/2}$ and Au $4f_{5/2}$.

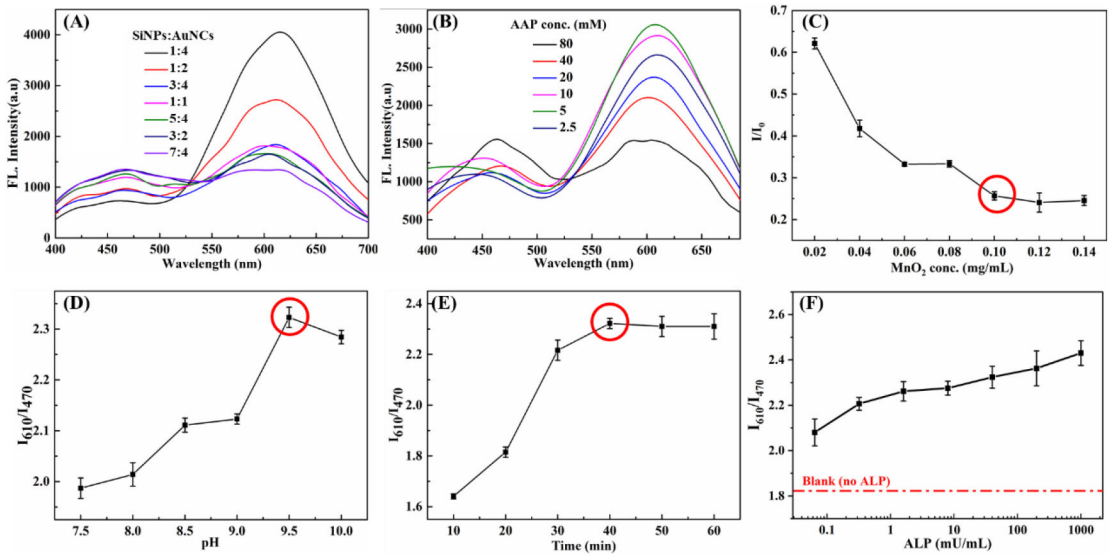

Fig. 6.

(A) Optimizing of ratios of SiNPs and AuNCs; (B) Optimizing of various concentrations of AAP with the 1 mU of ALP; (C) The signal inhibition with MnO_2, I0 and I was the value of I_{610}/I_{470} without and with MnO_2, respectively; Optimizing of (D) pH and (E) reaction time for ALP. The red circles indicate the optimized parameters that was chose for the development of RFIA; (F) Response of ALP by using optimized SAM system.

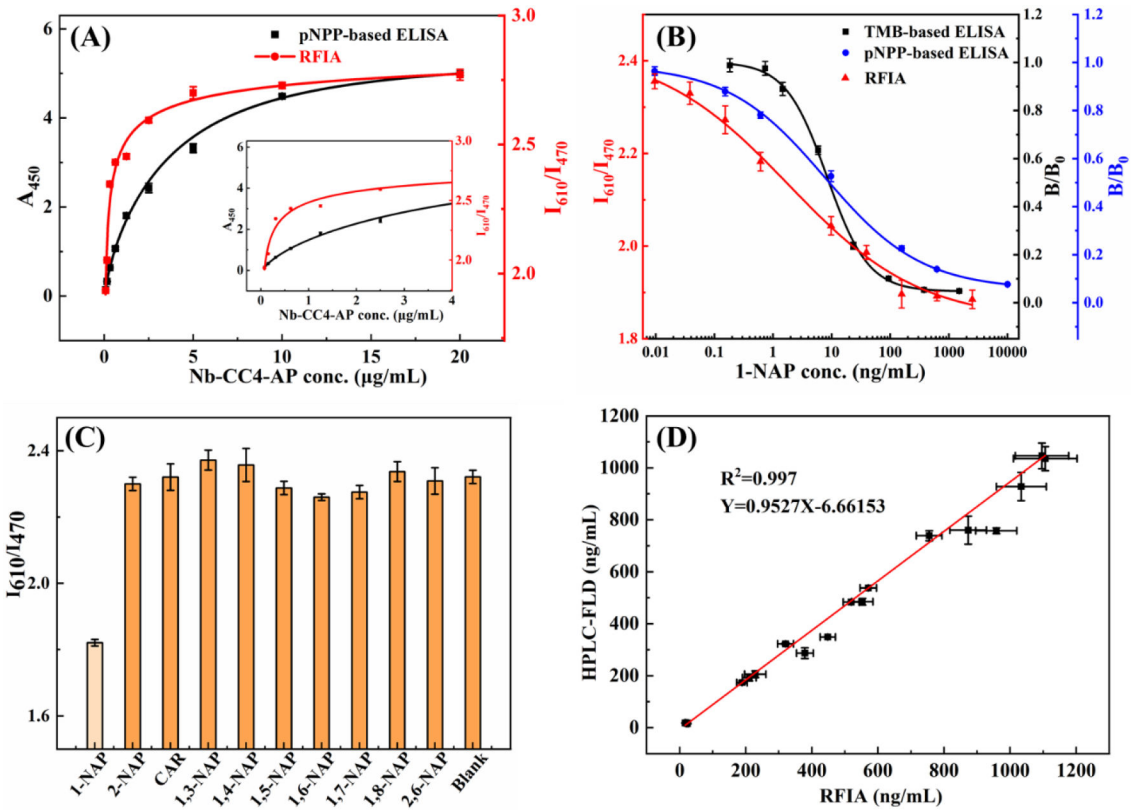

Fig. 7.

(A) The titer of pNPP-based ELISA and RFIA; (B) The calibration curve of TMB-based ELISA, pNPP-based ELISA and RFIA, with the IC_{50} value of 8.3 ng/mL, 7.6 ng/mL, and 1.8 ng/mL, respectively; and with the LOD of 1.4 ng/mL, 0.1 ng/mL, and 0.01 ng/mL, respectively; (C) Response of analogues for RFIA; (D) Correlation between HPLC-FLD and RFIA.

Table 1

The comparison of rapid detection method for 1-NAP

Antibody	Method	Substrate	IC_{50} (ng/mL)	Linear Range (ng/mL)	LOD (ng/mL)	Reference
ND[a]	Fluorescent Sensor	ND	ND	7×10^3~3×10^6	7×10^3	(Qin and Yan, 2018),
pAb	ELISA	TMB	72	10~1000	10	(Kramer et al., 1994)
mAb	ELISA	TMB	11.2	4.0~31.4	2.2	(Chen et al., 2020)
Nb-CC4	ELISA	TMB	8.3	2.7~25.6	1.4	This work
ALP-Nb-CC4	ELISA	pNPP	7.6	0.5~107.8	0.1	This work
ALP-Nb-CC4	RFIA	AAP & SAM system	1.8	0.05~66.4	0.01	This work

[a]ND, no data.

Table 2

Titers for anti-interference test (n=3)

Method	Titer[a] (Mean±SD[b])	CV[c] (%)
TMB-based ELISA	1.02±0.09	8.8
pNPP-based ELISA	1.08±0.06	5.6
RFIA	2.36±0.08	3.4

[a]Titers of different methods were measured with microplate reader. For TMB and pNPP-based ELISA, titers were measured at the absorbance of 405 nm and 450 nm, respectively. For RFIA, titer was calculated by I_{610}/I_{470}.

[b]SD, standard deviation.

[c]CV, coefficient of variance, which was obtained from intra-assay.